


Electrical spectroscopy of defect states and their hybridization in monolayer MoS₂

Received: 13 January 2022

Accepted: 15 December 2022

Published online: 03 January 2023

 Check for updates

Yanfei Zhao ^{1,2}, Mukesh Tripathi ^{1,2}, Kristiāns Čerņevičs ³, Ahmet Avsar ^{1,2,4}, Hyun Goo Ji^{1,2}, Juan Francisco Gonzalez Marin ^{1,2}, Cheol-Yeon Cheon^{1,2}, Zhenyu Wang^{1,2}, Oleg V. Yazyev ³ & Andras Kis ^{1,2} 

Defects in solids are unavoidable and can create complex electronic states that can significantly influence the electrical and optical properties of semiconductors. With the rapid progress in the integration of 2D semiconductors in practical devices, it is imperative to understand and characterize the influence of defects in this class of materials. Here, we examine the electrical response of defect filling and emission using deep level transient spectroscopy (DLTS) and reveal defect states and their hybridization in a monolayer MOCVD-grown material deposited on CMOS-compatible substrates. Supported by aberration-corrected STEM imaging and theoretical calculations, we find that neighboring sulfur vacancy pairs introduce additional shallow trap states via hybridization of individual vacancy levels. Even though such vacancy pairs only represent ~10% of the total defect concentration, they can have a substantial influence on the off currents and switching slopes of field-effect transistors based on 2D semiconductors. Our technique, which can quantify the energy states of different defects and their interactions, allows rapid and nondestructive electrical characterization of defect states important for the defect engineering of 2D semiconductors.

Two-dimensional (2D) semiconducting materials such as MoS₂ are considered as one of the most promising material platforms for future electronic devices^{1,2}. Observation of high on/off current ratios and reduced standby currents at nm-scale gate lengths, together with high mobility make them promising candidates for extending Moore's law^{3,4}. At the same time, their unique physical properties make them appealing for next-generation applications, including spintronics, valleytronics, twistrionics and straintronics, which are considered as frontier replacements for beyond-the-Moore's era^{5–10}. Even though large-scale synthesis of these materials in a scalable fashion has been achieved by metal-organic chemical vapor deposition (MOCVD)^{11–14}, the material quality and device performance are lagging behind expectations due to the ubiquitous structural defects^{15,16}, which can create unexpected doping¹⁷, increase charge carrier scattering and

introduce hopping transport¹⁸ as well as degrade the efficiency of optoelectronic devices through nonradiative recombination¹⁹. To accelerate the process of realizing optimal devices with desirable electrical performance, defects in these materials need to be well understood as a first step towards reducing their concentration and impact on device performance.

There are several techniques available for characterizing defects in 2D materials, with their own advantages and disadvantages. For instance, high-resolution transmission electron microscopy (TEM) and scanning tunneling microscopy (STM) provide direct visualization of atomic defects^{15,16,20}. However, the small and localized field of view together with the required material transfer process onto non-conventional (holey or conductive) substrates result in additional complications when compared with a regular device in which the 2D

¹Institute of Electrical and Microengineering, École Polytechnique Fédérale de Lausanne (EPFL), CH-1015 Lausanne, Switzerland. ²Institute of Materials Science and Engineering, École Polytechnique Fédérale de Lausanne (EPFL), CH-1015 Lausanne, Switzerland. ³Institute of Physics, École Polytechnique Fédérale de Lausanne (EPFL), Lausanne, Switzerland. ⁴Department of Materials Science and Engineering, National University of Singapore, Singapore 117575, Singapore. ✉e-mail: andras.kis@epfl.ch

material has undergone significant processing, which could alter its composition and defect concentration. In addition, the inevitable electron beam-induced damage makes TEM a destructive method. Alternatively, optical spectroscopy methods such as Raman^{21,22}, X-ray photoelectron²³, and photoluminescence spectroscopies²⁴, as well as electrical characterization techniques like capacitance-voltage (C-V) measurements²⁵ can give insights into the presence of disorder in the material integrated into a device, but are often qualitative in nature. The development of a reliable and practical method, capable of performing precise analysis on regular device architectures is required for 2D materials.

Deep level transient spectroscopy (DLTS)²⁶, a characterization technique for studying electrically active defects, based on the filling and emptying of trap states via voltage pulses, has been extensively employed for defect characterization of traditional semiconductors due to its extremely high sensitivity and wide detection ranges in the band gap^{26–28}. It provides information that can be used for defect identification and fingerprinting, including the defect types (n/p), trap concentrations, activation energies, capture cross sections, emission rates, etc. Despite numerous advantages, this method has so far not been applied to 2D semiconductors. The most common geometry for DLTS measurements is a vertical Schottky diode or a p-n junction in which voltage pulses are used to modulate the width of the depletion region. This is however not possible to achieve in monolayer 2D semiconductors because of their atomic-scale thickness, and as a result, only bulk MoS₂ has been studied using DLTS^{29,30}. The application of this technique to technologically relevant monolayer crystals grown using MOCVD or a similar technique remains unexplored.

Here, we extend the range of applications for DLTS to 2D semiconductors and report DLTS measurements on a single-layer TMDC-based device by employing the metal-insulator-semiconductor (MIS)

configuration and adapting the method to the 2D geometry. We find electrical signatures related to sulfur vacancies and detect hybridized defect states due to neighboring sulfur vacancy pairs. These states lie closer to the conduction band edge than the previously considered sulfur vacancy states and have a significant contribution to the density of states and could negatively impact the mobility, on/off ratio and switching slope of field-effect transistors based on 2D semiconductors. Our findings demonstrate that DLTS is a powerful and versatile technique for the non-destructive electrical defect characterization of 2D semiconductors, which could be used for benchmarking the material quality, making it essential for defect engineering and mitigation.

Results

DLTS method for monolayer semiconductors

Our single-crystal MoS₂ is grown on a c-plane sapphire substrate in a hot-wall MOCVD reactor. Supplementary Fig. 1a shows its triangular shape with a large lateral size and sharp crystal edges. Raman spectroscopy confirms the single-layer thickness of the as-grown material (Supplementary Fig. 1b). Figure 1a shows the metal-insulator-semiconductor (MIS) structure used throughout this work. Our device is fabricated on top of the sapphire substrate to eliminate any background-related charges and noise and to minimize stray and background capacitance. We use a gate stack composed of a local Ti/Au (2 nm/30 nm) bottom gate and a high- κ dielectric HfO₂ (30 nm thick) to effectively modulate the electrical field and tune the conductivity of the MoS₂ flake. Finally, we pattern the top contact composed of 80 nm of Au contacting the perimeter of the MoS₂ crystal (Fig. 1b inset) to achieve ohmic-like contacts for effective charge carrier injection.

Prior to DLTS measurements, we first perform a basic capacitance-voltage (C-V) characterization to evaluate the device performance in

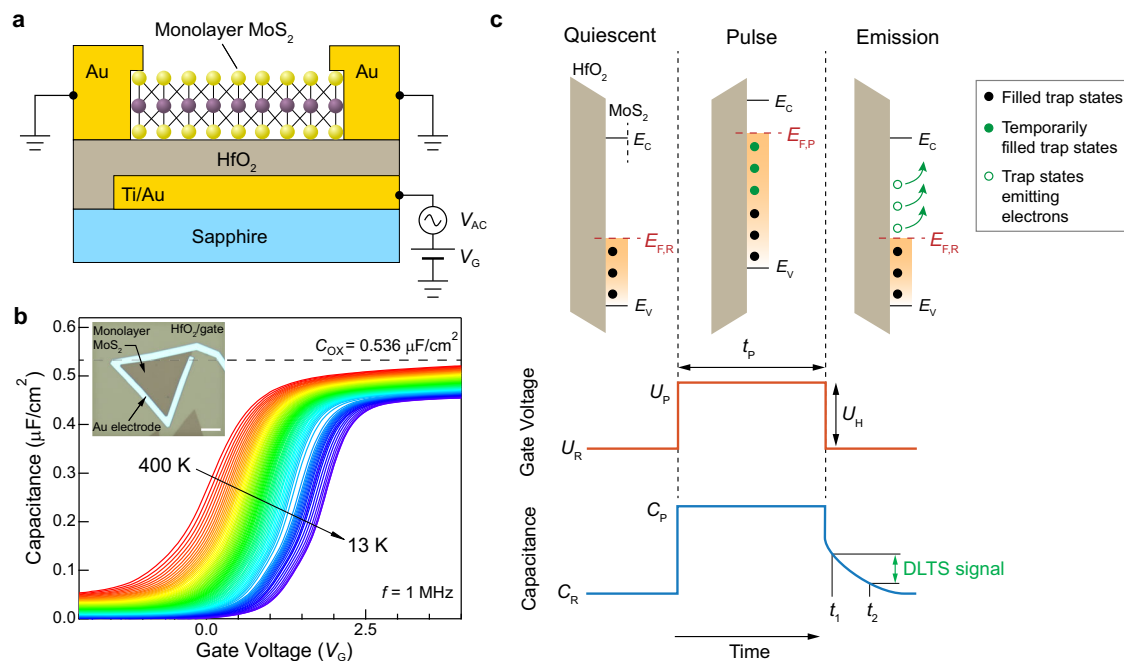


Fig. 1 | Device configuration for deep-level transient spectroscopy (DLTS) measurements. **a** The metal-insulator-semiconductor (MIS) capacitor device configuration used for capacitance-voltage (C-V) and DLTS measurements. **b** Temperature-dependent C-V curve measured using a 1 MHz, 50 mV oscillating signal V_{AC} superposed on the DC gate voltage V_G . The horizontal, dotted line marks the saturating capacitance from the oxide (C_{OX}). The inset shows the optical image of the MIS capacitor device. The scale bar is 10 μm long. **c** A schematic diagram showing the band alignment, the carrier interaction with trap states, and the voltage and capacitance change during the DLTS measurement. The orange-shaded

regions represent the MoS₂ band below the Fermi level E_F . The green arrows represent the carrier emission process. In panel **c**, E_C and E_V represent respectively the energy level of conduction band and valence band, while $E_{F,R}$ and $E_{F,P}$ are Fermi levels in the reference (quiescent) and pulsed states, respectively. The pulse parameters are respectively the reference voltage U_R , the pulse voltage U_P , the pulse height U_H , and the pulse width t_p , and C_R and C_P represent the device capacitances in the reference (quiescent) and pulsed states. The DLTS signal is measured as the capacitance difference between the rate window t_1 and t_2 .

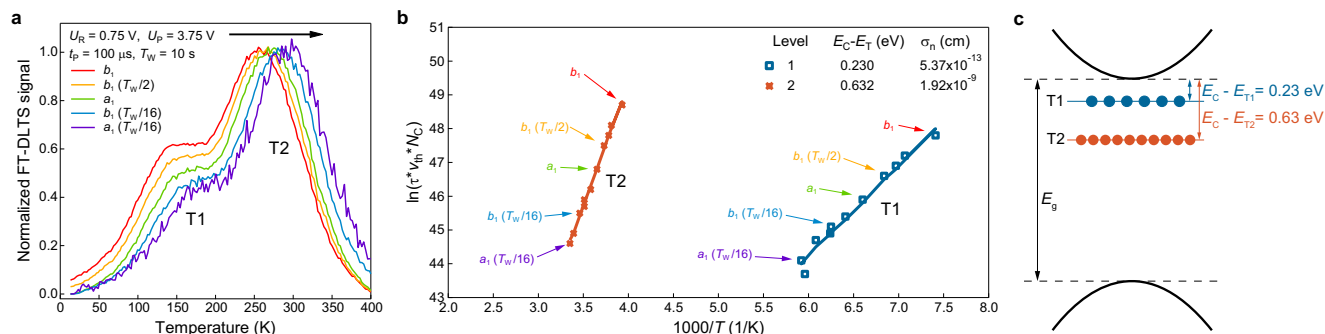


Fig. 2 | Defect levels in single-crystal MoS₂ characterized by DLTS. **a** Normalized Fourier transform DLTS signal measured using different correlation functions, showing two types of defect states (T1 and T2). Here, b_1 , $b_1(T_W/2)$, a_1 , $b_1(T_W/16)$, $a_1(T_W/16)$ are 5 correlation functions used as examples to demonstrate peak shifts with different rate windows. The reference voltage U_R is fixed at 0.75 V, pulse voltage U_p at 3.75 V, pulse width t_p at 100 μ s, and the period width T_W at 10 s. **b** Arrhenius fits obtained from panel a, showing the two detected trap states. Here,

the table in the inset lists the activation energy $E_C - E_T$ and the capture cross section σ_n of T1 and T2 trap states, obtained from the slope and intersect of the two Arrhenius curves. **c** A schematic diagram showing the relative energy positions (E_{T1} and E_{T2}) and trap concentrations (indicated by the number of circles) of the two detected defect states in the band gap. E_g is the band gap energy of monolayer MoS₂.

the steady state. We sweep the back-gate voltage (V_G) in the ± 5 V range with a 50 mV, 1 MHz oscillating signal (V_{AC}) connected in series, while measuring the capacitance between the bottom gate and the top contact (Fig. 1a, b). Our MOCVD-grown MoS₂ device exhibits n-type conductivity with a threshold voltage (V_{TH}) of 0.65 V at room temperature, taken as the V_G with half of the oxide capacitance ($1/2 C_{OX}$) as previously suggested^{31,32}. The rapid capacitance saturation indicates an effective Fermi level (E_F) tuning by the gate voltage. The small frequency dispersion and the low series resistance (Supplementary Note 2) indicate high-quality devices.

Traditional DLTS measurements rely on the modulation of the depletion region in a semiconductor device (Supplementary Note 3 and refs. 26, 30), typically a vertical Schottky diode. The atomic-scale thickness of monolayer 2D semiconductors however prevents the formation of the depletion width in the vertical direction. Instead, by using the MIS configuration shown in Fig. 1a, we can modulate the trap filling and extend the DLTS method to monolayer semiconductors by tuning the surface Fermi level by the back-gate voltage V_G ^{33,34}. Another disadvantage of traditional DLTS geometries based on a vertical Schottky diode is their inability to probe devices in the accumulation regime, since a forward-biased device would carry current. This is not the case for MIS devices where tuning the Fermi level will result in trap filling in both the depletion and accumulation regions.

The modification of the DLTS method for studying monolayer semiconductors is illustrated in Fig. 1c. The device is first held in a quiescent depletion condition, with constant reference bias (U_R) and capacitance (C_R) values. By applying a voltage pulse (U_p) with a height U_H and duration t_p , the Fermi level ($E_{F,R}$) is raised to a shallower position ($E_{F,p}$), allowing the temporary filling of trap states between $E_{F,R}$ and $E_{F,p}$, resulting in an increased capacitance, up to C_p . The reference voltage (U_R) and the pulse voltage (U_p) determine, respectively the lower and upper boundary of the energy range within which we can detect the trap states. At the end of the pulse, the filled states start emitting electrons with a time constant (τ) and an emission rate (e_n), as indicated by the green arrows, resulting in an exponential capacitance decay. The difference $\Delta C = C(t_1) - C(t_2)$ between capacitances measured at different times t_1 and t_2 is the DLTS signal²⁶, with a rate window defined by t_1 and t_2 . Changing the temperature modifies the trap emission rates, giving rise to temperature dependence in the DLTS spectra such as the one shown in Fig. 2a and Supplementary Fig. 5, with characteristic peaks related to individual trap levels. Here, we use the Fourier transform (FT) DLTS

technique in which the time-dependent capacitance decay is expressed in terms of Fourier coefficients³⁵.

In order to quantitatively relate the defect properties to the temperature-dependent DLTS signal, we first derive (Supplementary Note 5) a modified Arrhenius function for the 2D geometry (Eq. (1) and Fig. 1c) to describe how the temperature (T), the trap activation energy ($E_C - E_T$), and the capture cross section (σ_n) influence the carrier emission rate and lifetime:

$$\ln(\tau \cdot T^3 \cdot K_{2D}) = \frac{E_C - E_T}{k_B} \cdot \frac{1}{T} - \ln(\sigma_n) \quad (1)$$

Here, E_C is the conduction band minimum, E_T is the energy level of the trap state, k_B is the Boltzmann constant, and K_{2D} is a constant value independent of temperature and trap energy, equal to $2.74 \times 10^{16} \text{ cm}^{-1} \text{ s}^{-1} \text{ K}^{-3/2}$. By plotting $\ln(\tau \cdot T^3 \cdot K_{2D})$ as a function of $1/T$, we can directly obtain $E_C - E_T$ and σ_n values through a linear fit. Equation (1) is similar to the 3D Arrhenius function (Supplementary Note 5), but with a different temperature exponent, due to the dimensional difference in thermal velocity (v_{th}) and the effective electron density of states (N_C). The capture cross-section σ_n , representing the capability of a trap state to capture electrons and holes, has a dimension of length for a single-layer device, rather than area as for a bulk semiconductor. In general, σ_n is a material parameter which can be influenced by multiple factors such as the defect size and Coulomb charging³⁶.

Trap state-level determination by DLTS

To identify the optimal pulsing conditions and investigate different emission conditions, we first carry out a series of DLTS measurements at room temperature with various pulse parameters (Supplementary Note 6). Subsequently, we perform the DLTS measurement as a function of temperature to extract the trap characteristics using Eq. (1). Figure 2a and Supplementary Fig. 7 show the normalized temperature scan of a series of transient signals at different rate windows, accessed by 11 correlation functions (a_1 , b_1 , $b_1(T_W/2)$, etc.) which correspond to the following Fourier coefficients obtained from the Fourier series of the capacitance transient³⁵:

$$a_n(\tau) = \frac{2\Delta C}{T_W} e^{-\frac{t_0}{\tau}} \left(1 - e^{-\frac{T_W}{\tau}}\right) \frac{1/\tau}{\frac{1}{\tau^2} + n^2 \omega^2} \quad (2)$$

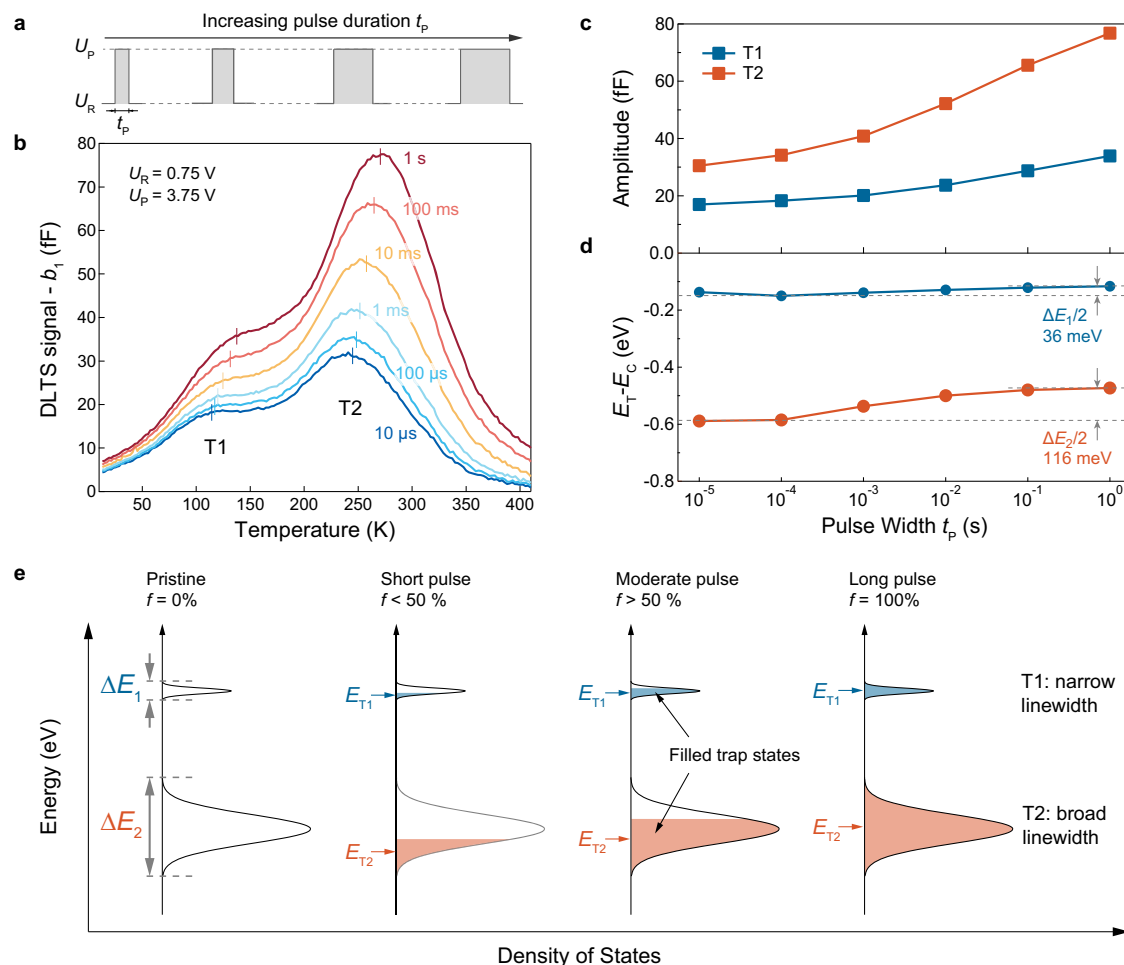


Fig. 3 | Defect level linewidth and control of defect filling. **a** A simple scheme and **b** the DLTS temperature sweep at various pulse width t_p values. Here, the reference and pulse voltages are fixed at 0.75 V and 3.75 V respectively. **c** Change of peak amplitudes and **d** measured trap energies with respect to t_p . Each data point is obtained from the two peak positions in panel b. The gray dash line in panel d marks

the shifting of trap energies from short to long pulses. **e** A schematic diagram showing the measured E_T values changing with the trap-filling ratio (f) for T1 and T2 states. The blue and orange shaded regions represent the part of T1 and T2 density of states (DOS) filled by charge carriers. ΔE_1 and ΔE_2 represent the total energy linewidth for T1 and T2 defects respectively.

and

$$b_n(\tau) = \frac{2\Delta C}{T_W} e^{-\frac{t_0}{\tau}} (1 - e^{-\frac{T_W}{\tau}}) \frac{n\omega}{\frac{1}{\tau^2} + n^2\omega^2} \quad (3)$$

where n is the order of the Fourier series, T_W the measurement window, $\omega = 2\pi/T_W$ and ΔC is the amplitude of the capacitance transient.

We can observe two prominent FT-DLTS peaks in Fig. 2a, related to two distinct trap states in our MoS₂ device that we label T1 and T2. Taking the τ value for each correlation function and the corresponding peak temperature, we plot the Arrhenius curves, and extract the trap activation energy and capture cross section for both states as shown in Fig. 2b. We find that T1 corresponds to a shallower state, located 0.230 eV below E_C while T2 is related to a deeper state at 0.632 eV below E_C , Fig. 2c. The relative trap concentrations are related to peak heights²⁶, indicating the prevalence of T2 over T1. Due to its higher prevalence and similarity with previously reported trap energy levels^{15,16}, we tentatively assign the T2 trap state to sulfur vacancies (V_S). The extracted capture cross-section of T2 is 1.92×10^{-9} cm, similar in size to a vacancy site and comparable to the square root of the σ_n value obtained from its exfoliated, bulk counterpart³⁰. On the other hand, the energy level of the T1 state does not match with those commonly associated with single (V_S) or double (V_{S_2}) sulfur vacancies^{15,16} and therefore requires

further investigation outlined here using STEM imaging and density-functional theory (DFT) calculations.

Trap state energy linewidth determination by DLTS

In addition to quantifying the trap level position inside the band gap, DLTS can also provide additional defect fingerprinting information in the form of the trap state energy linewidth. It can be extracted from the DLTS measurements by modifying the voltage pulse width t_p and/or the voltage pulse amplitude U_p , resulting in different levels of trap filling reflected in the DLTS signal amplitude, shown on Fig. 3 and Supplementary Figures 8 and 9. Amplitudes of both T1 and T2 peaks (Fig. 3b) increase with t_p (Fig. 3c) as a result of increased trap state filling. By performing Arrhenius fitting for each of the DLTS curves in Fig. 3b, we can extract the variation of trap activation energy $E_C - E_T$ with t_p (Fig. 3d). The effective trap energy level remains practically constant for the T1 state (36 meV shift) but exhibits a larger shift closer to the band edge for the T2 peak (116 meV shift). Similar trends are also observed with increased U_p values but the influence is less significant (Supplementary Fig. 9).

We explain this behavior by considering the trap state energy linewidth (ΔE) as illustrated on Fig. 3e. The trap activation energy $E_C - E_T$ extracted from DLTS measurements corresponds to the average energy of the filled trap states shown as the shaded regions. For completely filled traps, this would correspond to the ideal $E_C - E_T$ value,

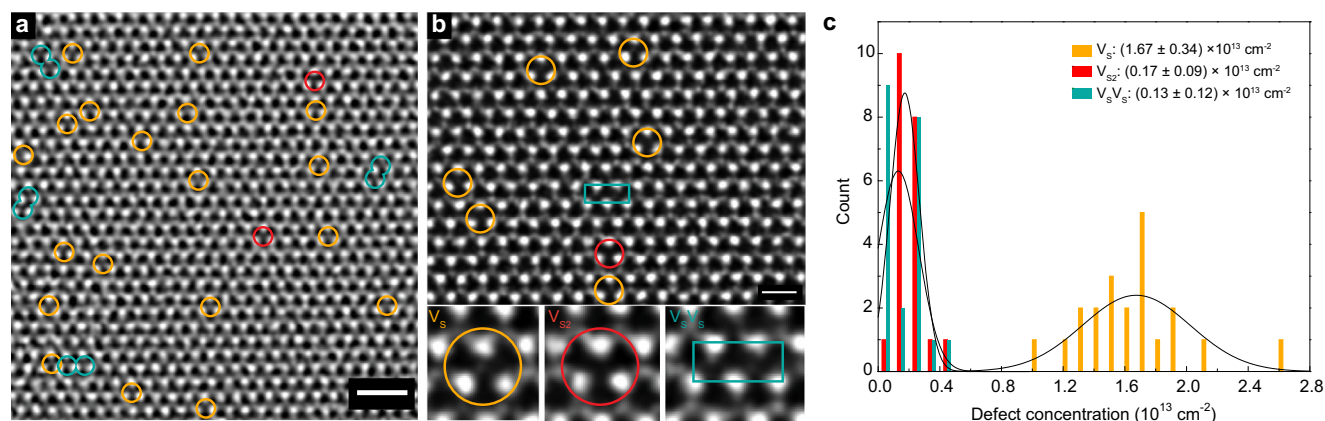


Fig. 4 | Atomic defects characterized by scanning transmission electron microscope (STEM). **a, b** Filtered STEM image showing different types of defects. Orange and red circles highlight single (V_S) and double (V_{S_2}) sulfur vacancy defects, respectively, while the turquoise green box marks two V_S right next to each other

($V_S V_S$). **c** Histogram (bar shape) and corresponding Gauss fit (solid line) of V_S , V_{S_2} , $V_S V_S$ concentrations calculated from 21 pristine regions of the as-grown single crystal. The scale bars in panels a and b are respectively 1 nm and 0.5 nm long.

while partially filled trap states would result in $E_C - E_T$ values shifted to lower energies³⁷. The energy linewidth ΔE of a given trap state can then be estimated as the double of the $E_C - E_T$ shift from the values obtained for empty ($f = 0$, short t_p) to complete trap-filling conditions ($f = 100\%$, long t_p), as shown in Fig. 3e. We expect that states with a narrower linewidth would show a smaller variation with t_p , such as in the case of T1. States with a wider distribution would be more sensitive to t_p . This is the case for the T2 trap which shows a saturating energy shift for the longest pulse duration ($t_p = 1$ s) achievable in our setup. We extract from our measurements effective linewidths of $\Delta E_1 = 72$ meV for the T1 state and $\Delta E_2 = 232$ meV for the T2 state. Such linewidth estimations further reinforce DLTS as an important defect characterization technique since this information cannot be accessed *via* STEM or electrical transport measurements.

Defect characterization by STEM

To investigate the origin of the two defect states detected by DLTS measurements, we perform aberration-corrected STEM on the as-grown MoS₂. The wide-field annular dark field (ADF)-STEM image in Fig. 4a shows the atomic structure of free-standing monolayer MoS₂, where Mo ($Z = 42$) atoms appear brighter in comparison to the S2 ($Z = 32$) atoms owing to their Z-contrast dependency. To minimize possible errors caused by the localized field of view, we perform ADF-STEM imaging on 21 pristine regions. In all regions, we observe only sulfur vacancy defects in our material and do not observe any Mo vacancies or antisite defects that were previously reported for CVD-grown materials¹⁵, implying excellent growth conditions in our MOCVD method. In Fig. 4a, b, we label the three most common vacancy configurations: isolated single sulfur vacancy (V_S), isolated double sulfur vacancy (V_{S_2}), and two single sulfur vacancies next to each other ($V_S V_S$), as highlighted by orange, red, and turquoise green colored circles and boxes, respectively. The concentration histogram and the average defect densities of V_S , V_{S_2} , and $V_S V_S$ measured from 21 pristine regions are presented in Fig. 4c. These values are of the same order of magnitude as in exfoliated samples, indicating the high quality of our MoS₂ crystal³⁸. In addition, we observe an apparent sulfur vacancy creation under the electron-beam irradiation, allowing us to estimate the intrinsic defect concentrations (Supplementary Note 9)³⁹. These STEM results confirm that the two defects inferred from the DLTS measurements are both related to sulfur vacancies.

DFT modeling and hybridized defect states

Our DFT calculations show that single sulfur vacancies (V_S) (Fig. 5a), the dominant defect type identified by ADF-STEM imaging, exhibit

energy levels 0.5–0.6 eV below E_C , in line with the T2 energy measured by DLTS and other reported calculations^{15,16}. We note that the band gap energy is systematically underestimated by the Perdew-Burke-Ernzerhof (PBE) functional (1.68 eV) and therefore, the deviation of ~ 0.1 eV between DLTS and DFT is within the error range (for more discussion please refer to Supplementary Note 10). Strikingly, with top and bottom sulfur atoms missing, the double sulfur vacancy defect (V_{S_2}) has nearly the same energy levels as V_S inside the gap. In addition to the in-gap state, V_{S_2} is also predicted to have another defect level located inside the conduction band (Supplementary Fig. 12)¹⁵, which, however, is outside the detection range of our DLTS technique²⁶. Despite the large hybridization-induced splitting of around 0.6 eV that pushes one of the states into the conduction band, we still observe similar defect energy positions and overlapping density of states (DOS) with V_S (Fig. 5a, b) inside the gap. We note that the charge densities associated with both V_S and V_{S_2} defect states (Fig. 5d, e) show a comparable localized behavior with the three closest Mo atoms displaying the largest density. Small differences can be observed in the side view: while the charge density of the V_S defect states shows a slight localization preference towards the side of the missing atom, the V_{S_2} density is mirror-symmetric along the Mo atoms. Furthermore, we do not observe meaningful differences in the Mo-S bond length (2.41 Å) modulation near the defects as in both cases the Mo-S bonds lengths are within the range of 2.38–2.45 Å. This makes it difficult to distinguish between these two trap types, as also revealed by the apparent peak width and the relatively large full-width at half maximum (FWHM) in DLTS measurement (Fig. 2a). These results clearly verify the origin of the T2 state to be V_S and V_{S_2} defects, as well as excluding their possible relation with the T1 state.

According to the DFT calculations, four in-gap hybridized defect states are created for the first nearest neighbor sulfur vacancy pairs ($V_S V_S$, INN), with their energies distributed between 0.2 eV and 0.7 eV below E_C (Fig. 5c). The splitting between the hybridized defect states is approximately 0.4 eV, making it smaller than the splitting observed in V_{S_2} and hence leading to additional in-gap states close to the conduction band edge. Interestingly, the charge density of, for example, the first (Fig. 5f) and third (Supplementary Fig. 15d) in-gap states clearly show a different localization pattern in comparison to the V_S and V_{S_2} defects. Most importantly, we can see that a large part of the charge density is now also delocalized over the neighboring sulfur atoms and even more distant Mo atoms. Although the local bond length modulations show minor differences with the V_S and V_{S_2} defects, we note that the minimum Mo-S bond length (2.36 Å) is observed exactly in the $V_S V_S$ configuration. Evidently, the reduced interaction of the two in-

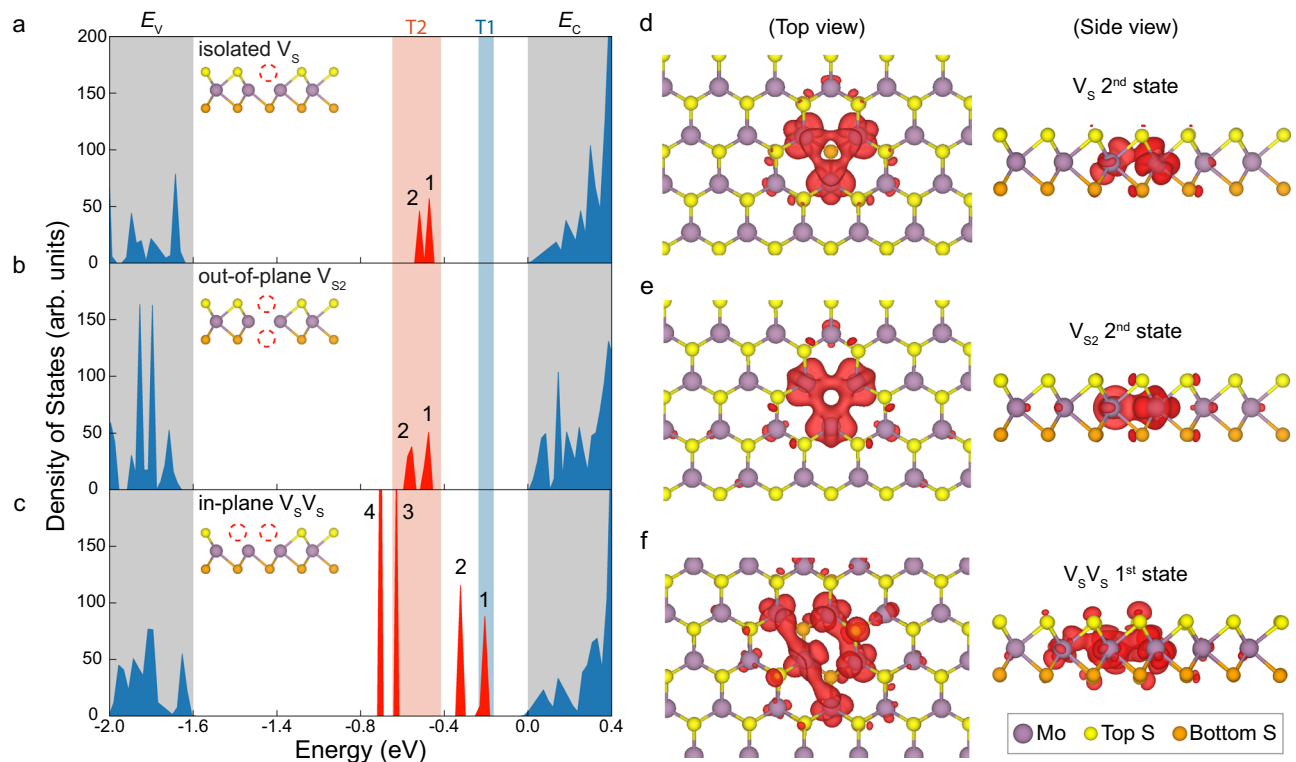


Fig. 5 | Defect energy levels and hybridization calculated by density functional theory (DFT). **a–c** Calculated density of states (DOS) of **a**, an isolated single sulfur vacancy (V_S), **b**, double sulfur vacancies (V_{S_2}), and **c**, a neighboring sulfur vacancy pair on the same lattice plane ($V_S V_S$). Inset shows the side view of the vacancy positions in MoS_2 atomic lattice. The shaded gray regions mark out the valence and conduction bands. The calculated in-gap defect states are indicated in red, and the blue and orange shaded regions are respectively the T1 and T2 defect states

measured by DLTS. Here, the band gap energy E_g is predicted to be 1.68 eV using the Perdew-Burke-Ernzerhof (PBE) functional. The two states for V_S or V_{S_2} belong to a single level but include the spin-orbit coupling. **d–e** Top and side view of the charge density distribution of the 2nd in-gap state for **d**, V_S and **e**, V_{S_2} defects as marked in panels **a–b**. **f** Top and side view of the charge density distribution of the 1st in-gap states for the neighboring $V_S V_S$ pair shown in panel **c**.

plane as opposed to the two out-of-plane vacancies lead to a type of hybridization, where 4 distinguishable in-gap states appear. In addition, we also note that the energies of these hybridized states highly depend on the distance between the neighboring sulfur vacancies (Supplementary Fig. 14). Continuously increasing the distance would lead to the convergence of these four defect levels into two levels resembling the DOS of V_S . Comparing to the measured $E_C - E_T$ value of 0.230 eV by DLTS, we attribute the T1 trap to the shallower doublet state created by $V_S V_S$ that has been directly observed in STEM (Fig. 4a, b). We expect a slight contribution of $V_S V_S$ to the T2 trap as well, but their influence is less significant compared to the more abundant isolated V_S . We exclude other defect types based on the discussion in Supplementary Note 10.

Sulfur vacancy creation by Ar plasma probed by DLTS

In order to verify the origin of DLTS signal from sulfur vacancies, we performed additional measurements on a similar MoS_2 MIS device that is exposed to mild Ar plasma to create a higher concentration of defects (Supplementary Note 11). After 4 seconds of mild plasma treatment, we observe an increased DLTS signal of around 25%, as well as the right shift of the DLTS peaks towards higher temperature, which indicates an increase of sulfur vacancy concentration, especially the creation of neighboring sulfur vacancies (Supplementary Fig. 16). These results demonstrate a correlation of V_S concentration variation with the DLTS signals and further confirm the attribution of the DLTS signal to sulfur vacancies.

Moreover, additional experiments using transferred metal contacts demonstrate the same dominant DLTS peak associated with the T2 (V_S and V_{S_2}) state, which excludes the contact fabrication as the

source of defects in our monolayer MoS_2 MIS devices (Supplementary Note 12). Besides, a control experiment using the metal-insulator-metal (MIM) structure further eliminate the influence of oxide or parasitic capacitances on our DLTS spectra (Supplementary Note 13).

Discussion

Defects in 2D materials are usually considered independent of each other and their influence on electrical performance are studied individually. In monolayer MoS_2 , the most common defect, the single sulfur vacancy (V_S) is predicted to create only one deep state ($E_C - E_{T_2} \sim 0.5$ eV) in the band gap, as also confirmed experimentally by STM spectroscopy³⁸. In addition to this state, we also resolve a previously overlooked shallower defect level ($E_C - E_{T_1} \sim 0.2$ eV) created by the hybridization between neighboring pairs of V_S ($V_S V_S$). Since these states lie closer to the conduction band edge, they will significantly shift the threshold voltage and decrease the subthreshold slope in field-effect transistors. In addition, compared to the single defect level created by V_S , the four hybridized defect levels associated with $V_S V_S$ pairs can substantially increase the chance of defect-assisted recombination, which could lead to diminished quantum yield in optoelectronic devices. Even though their concentration corresponds to only 10% of isolated V_S (Fig. 4c), the neighboring $V_S V_S$ pairs give rise to a distinct DLTS peak (T1) with 60% of the T2 peak height (Fig. 2a), indicating a significantly larger density of in-gap states than for their isolated counterparts. This increased DOS is due to the hybridization of neighboring sulfur defects as seen from the charge density plots (Fig. 5f and Supplementary Figure 14–15). Therefore, to achieve high quality devices with minimum density of states and narrowest energy linewidth, defect hybridization needs to be largely avoided. For that, a

minimum distance of $\sim 8.44 \text{ \AA}$ (4NN in Supplementary Fig. 14) needs to be maintained between sulfur vacancies, corresponding to a maximum defect concentration of $3.5 \times 10^{13} \text{ cm}^{-2}$.

To summarize, we demonstrate the adaptation of the DLTS measurement technique to a single-layer, MOCVD-grown MoS_2 crystal using a CMOS compatible device geometry. This allows us to identify a shallow state (T1) induced by the hybridization of neighboring sulfur vacancy pairs on the same lattice plane, supported by STEM imaging and DFT calculations. Capability of energy linewidth detection by DLTS measurements is also demonstrated, confirming the narrow bandwidth of the hybridized shallow state, as well as considerable energy broadening of V_S traps. Considering the high sensitivity of DLTS measurements and its applicability to capacitor-based devices, such as field-effect transistors, our study provides a pathway for a comprehensive understanding of atomic defects and their electrical properties in 2D semiconductors in the single-layer limit. We expect the future application of DLTS technique in other 2D materials to enrich the defect library, to reveal unexplored defect characteristics and to enable effective defect engineering and mitigation. With the rapid progress of 2D materials towards future electronic device applications, the DLTS technique can serve as an efficient tool for defect characterization and device improvement.

Methods

Material synthesis

The MoS_2 single crystals are grown on c-plane sapphire chips in a 2-inch hot-wall tube reactor using the metal-organic chemical vapor deposition method. We first anneal the sapphire chips at $1000 \text{ }^\circ\text{C}$ in air for 2 h to create atomically smooth terraces for epitaxial growth⁴⁰. Prior to growth, 0.26 mol/L sodium chloride (NaCl) solution is spin-coated to suppress the nucleation and promote the crystal growth¹³. Molybdenum hexacarbonyl ($\text{Mo}(\text{CO})_6$) and hydrogen sulfide (H_2S) are used as the gas precursors to allow maximal control. Using 70 sccm Ar as the carrier gas, they are mixed with a molar ratio of 1:2009 in the tube furnace. The reaction takes place at $850 \text{ }^\circ\text{C}$ and is terminated with a cut-off of $\text{Mo}(\text{CO})_6$ precursor after 30 min of growth time. The furnace is then cooled down naturally to $150 \text{ }^\circ\text{C}$ with a continuous H_2S supply. The pressure is maintained at 850 mbar by a pressure regulator throughout the whole growth process. The optical microscopy image and Raman spectroscopy (Supplementary Fig. 1) confirm the monolayer thickness of the as-grown MoS_2 .

Sample transfer and STEM imaging

Atomic-scale annular dark-field scanning transmission electron microscopy (ADF-STEM) imaging of monolayer MoS_2 is performed using an aberration-corrected STEM (FEI Titan Themis 60–300), which is equipped with a Schottky X-FEG bright source, Cs double corrector and a monochromator. Before the STEM imaging, the as-grown MOCVD material is transferred onto a commercial silicon nitride TEM grid in DI water using the PMMA/gel-pak assisted method. Afterward, the grid is immersed in hot acetone and annealed in high vacuum for 10 h at $250 \text{ }^\circ\text{C}$ to remove the polymer resists. Imaging is performed at a low acceleration voltage of 80 kV , which is below the displacement knock-on damage of MoS_2 . The probe current is set to 18 pA for all the experiments. The semi-convergence angle of the electron probe is 20 mrad and at a 185 mm camera length, the angular range of the higher angular annular dark field (HAADF) detector is $49.5\text{--}198 \text{ mrad}$. Both images and series are acquired using short dwell time ($8 \text{ }\mu\text{s}$) for 512×512 pixels. Each image is captured within an exposure time of $< 3 \text{ s}$ and an e-beam dose rate of $< 10^6 \text{ e}^{-1}\text{nm}^{-2}\text{s}^{-1}$ to minimize the beam damage. Images from series (Supplementary Figs. 10 and 11) are aligned manually for the drift correction and used to calculate the S defect concentrations. To remove the electron probe-tails, images are processed using double Gaussian filtering.

MIS capacitor device fabrication

Sapphire wafer, instead of SiO_2/Si , is chosen as the device substrate due to its excellent insulating property, minimizing stray capacitance. The bottom gate is patterned on the wafer-scale using photolithography, followed by the deposition of 2 nm Ti and 30 nm Au using an e-beam evaporator. The insulating layer is composed of 30 nm of hafnium oxide (HfO_2) grown via atomic layer deposition (ALD) using TEMA ($\text{tetramethylammonium hydroxide}$) and water as precursors. After that, we use the PMMA/gel-pak assisted method to transfer the MOCVD-grown MoS_2 flakes onto the patterned substrate. Polymer residues are then dissolved in acetone and further removed by high vacuum annealing at $250 \text{ }^\circ\text{C}$ for 8 h. Finally, the top contact is patterned by e-beam lithography, and 80 nm Au as contact is deposited by e-beam evaporation. The contact between metal and MoS_2 flake is improved by annealing the devices at $200 \text{ }^\circ\text{C}$ for 3 h before the electrical measurements.

C-V characterization

C-V characterization is performed in high vacuum after in situ annealing at $120 \text{ }^\circ\text{C}$ for more than 30 h to remove any surface absorption or contamination. The frequency-dependent C-V curves (Supplementary Fig. 3) are measured at room temperature using a Keysight E4980A precision LCR meter. The oscillation voltage is fixed at 50 mV with varied frequencies from 1 kHz to 1 MHz . The back gate voltage is swept forward and backward in the range of $\pm 5 \text{ V}$ with a sweeping rate of 20 mV/s .

The temperature-dependent C-V curves (Fig. 1b and Supplementary Fig. 2) are measured using a Boonton 7200 capacitance meter embedded in the PhysTech DLTS system. We perform a C-V measurement every 5 K as the temperature is increased from 12 K to 400 K . The oscillation frequency is fixed at 1 MHz to improve the signal-to-noise ratio, and the sweeping range and speed are the same as described above.

DLTS characterization

The DLTS measurements are performed on a PhysTech FT-1030 system. Capacitance transient signals are digitalized through numerical Fourier transformation, which allows the acquisition of 28 discrete Fourier coefficients within a single temperature scan. Comparing to the conventional boxcar method, FT-DLTS guarantees a higher accuracy through noise suppression and automatic control of measurement parameters³⁵. Here, due to the monolayer nature of the material, the transient signal is on the scale of tens or hundreds of femtofarad (fF), resulting in a relatively low signal to noise ratio comparing to bulk semiconductors. Each temperature sweep of the DLTS is performed from 400 K to 13 K with an interval of 2.5 K . Variation of each pulsing parameter (Fig. 3 and Supplementary Fig. 9) is obtained during one temperature sweep to guarantee identical measurement conditions.

DFT calculations

Our first-principles calculations are performed at the density-functional theory level with spin-orbit coupling included as implemented in VASP⁴¹. The exchange-correlation potential is approximated by the generalized gradient approximation (GGA) using the semilocal Perdew-Burke-Ernzerhof (PBE) functional⁴². Electron-core interactions are described through the projector augmented wave (PAW) method^{43,44}, while Kohn-Sham wave functions are expanded in a plane-wave basis set with a cutoff on the kinetic energy of 400 eV . The integration over the Brillouin zone is carried out using a $3 \times 3 \times 1$ k-point mesh. All structures are subjected to periodic boundary conditions using a 5×5 supercell geometry, while a vacuum layer of 10 \AA perpendicular to the monolayer is used to prevent interaction between replica images. Atomic positions and lattice constants are optimized using the conjugate gradient method, where the total energy and

atomic forces are minimized. The convergence criterion for energy is chosen to be 10^{-5} eV and the maximum force acting on each atom is less than 0.01 eV/Å relaxation. For all the plotted figures, we set zero energy at the conductance band minimum to easily identify and compare the defect level positions.

Ar plasma treatment

The Ar plasma treatment is performed using a PICO low-pressure plasma system from Diener electronic. Before treating the target device, a series of plasma tests are conducted on the as-grown MoS₂ sample by varying the plasma power (15–30 W), the Ar gas flow rate (5–30 sccm), and the treatment duration (1–30 s). Raman spectroscopy is used to assess the material quality after the plasma treatment (similar to ref. 45), which allows us to obtain a mild and non-destructive plasma condition for the device treatment.

The mild plasma is generated by dispersing a 21 W RF power in a 6-inch-diameter vacuum chamber with a 15 sccm of Ar flow, where the MoS₂ device is kept for 7 seconds (3 second plasma rising time + 4 second exposure time). The MoS₂ MIS device used here for plasma irradiation is from another chip fabricated together with the devices presented in Figs. 1–3. The C-V and DLTS measurement are performed immediately after the Ar plasma irradiation and an in situ annealing at 120 °C for more than 30 h.

Transfer of metal contacts

80 nm Au contacts with a designed pattern are deposited on top of clean SiO₂/Si substrate using an e-beam evaporator, and then picked up by a small piece of poly-dimethylsiloxane (PDMS) capped with 15% weight of poly-propylene carbonate (PPC) in chloroform. Afterwards, the stack is transferred on top of patterned MoS₂/HfO₂/Au/sapphire substrate using a transfer stage capable of precise alignment. The detailed transfer process and optical microscope images are shown in Supplementary Fig. 17.

Data availability

The data that support the findings of this study are available in Zenodo at <https://doi.org/10.5281/zenodo.7389794>.

References

1. Wang, Q. H., Kalantar-Zadeh, K., Kis, A., Coleman, J. N. & Strano, M. S. Electronics and optoelectronics of two-dimensional transition metal dichalcogenides. *Nat. Nanotechnol.* **7**, 699–712 (2012).
2. Manzeli, S., Ovchinnikov, D., Pasquier, D., Yazyev, O. V. & Kis, A. 2D transition metal dichalcogenides. *Nat. Rev. Mater.* **2**, 1733 (2017).
3. Radisavljevic, B., Radenovic, A., Brivio, J., Giacometti, V. & Kis, A. Single-layer MoS₂ transistors. *Nat. Nanotechnol.* **6**, 147–150 (2011).
4. Li, M.-Y., Su, S.-K., Wong, H.-S. P. & Li, L.-J. How 2D semiconductors could extend Moore's law. *Nature* **567**, 169–170 (2019).
5. Mueller, T. & Malic, E. Exciton physics and device application of two-dimensional transition metal dichalcogenide semiconductors. *Npj 2D Mater. Appl.* **2**, 1–12 (2018).
6. Schaibley, J. R. et al. Valleytronics in 2D materials. *Nat. Rev. Mater.* **1**, 1–15 (2016).
7. Ahn, E. C. 2D materials for spintronic devices. *Npj 2D Mater. Appl.* **4**, 1–14 (2020).
8. Avsar, A. et al. Colloquium: Spintronics in graphene and other two-dimensional materials. *Rev. Mod. Phys.* **92**, 021003 (2020).
9. Andrei, E. Y. & MacDonald, A. H. Graphene bilayers with a twist. *Nat. Mater.* **19**, 1265–1275 (2020).
10. Bukharaev, A. A., Zvezdin, A. K., Pyatakov, A. P. & Fetisov, Y. K. Straintronics: a new trend in micro- and nanoelectronics and materials science. *Phys. -Uspekhi* **61**, 1175 (2018).
11. Kang, K. et al. High-mobility three-atom-thick semiconducting films with wafer-scale homogeneity. *Nature* **520**, 656–660 (2015).
12. Yu, H. et al. Wafer-Scale Growth and Transfer of Highly-Oriented Monolayer MoS₂ Continuous Films. *ACS Nano* **11**, 12001–12007 (2017).
13. Kim, H., Ovchinnikov, D., Deiana, D., Unuchek, D. & Kis, A. Suppressing Nucleation in Metal–Organic Chemical Vapor Deposition of MoS₂ Monolayers by Alkali Metal Halides. *Nano Lett.* **17**, 5056–5063 (2017).
14. Cun, H. et al. Wafer-scale MOCVD growth of monolayer MoS₂ on sapphire and SiO₂. *Nano Res* **12**, 2646–2652 (2019).
15. Zhou, W. et al. Intrinsic Structural Defects in Monolayer Molybdenum Disulfide. *Nano Lett.* **13**, 2615–2622 (2013).
16. Hong, J. et al. Exploring atomic defects in molybdenum disulfide monolayers. *Nat. Commun.* **6**, 6293 (2015).
17. Komsa, H.-P. et al. Two-Dimensional Transition Metal Dichalcogenides under Electron Irradiation: Defect Production and Doping. *Phys. Rev. Lett.* **109**, 035503 (2012).
18. Qiu, H. et al. Hopping transport through defect-induced localized states in molybdenum disulfide. *Nat. Commun.* **4**, 2642 (2013).
19. Lien, D.-H. et al. Electrical suppression of all nonradiative recombination pathways in monolayer semiconductors. *Science* **364**, 468–471 (2019).
20. Liu, X., Balla, I., Bergeron, H. & Hersam, M. C. Point Defects and Grain Boundaries in Rotationally Commensurate MoS₂ on Epitaxial Graphene. *J. Phys. Chem. C* **120**, 20798–20805 (2016).
21. Cançado, L. G. et al. Quantifying Defects in Graphene via Raman Spectroscopy at Different Excitation Energies. *Nano Lett.* **11**, 3190–3196 (2011).
22. Mignuzzi, S. et al. Effect of disorder on Raman scattering of single-layer MoS₂. *Phys. Rev. B* **91**, 195411 (2015).
23. Syari'ati, A. et al. Photoemission spectroscopy study of structural defects in molybdenum disulfide (MoS₂) grown by chemical vapor deposition (CVD). *Chem. Commun.* **55**, 10384–10387 (2019).
24. Nan, H. et al. Strong Photoluminescence Enhancement of MoS₂ through Defect Engineering and Oxygen Bonding. *ACS Nano* **8**, 5738–5745 (2014).
25. Zhu, W. et al. Electronic transport and device prospects of monolayer molybdenum disulfide grown by chemical vapour deposition. *Nat. Commun.* **5**, 3087 (2014).
26. Lang, D. V. Deep-level transient spectroscopy: A new method to characterize traps in semiconductors. *J. Appl. Phys.* **45**, 3023–3032 (1974).
27. Johnson, N. M., Ponce, F. A., Street, R. A. & Nemanich, R. J. Defects in single-crystal silicon induced by hydrogenation. *Phys. Rev. B* **35**, 4166–4169 (1987).
28. Omling, P., Weber, E. R., Montelius, L., Alexander, H. & Michel, J. Electrical properties of dislocations and point defects in plastically deformed silicon. *Phys. Rev. B* **32**, 6571–6581 (1985).
29. Gelczuk, Ł. et al. Probing Defects in MoS₂ Van der Waals Crystal through Deep-Level Transient Spectroscopy. *Phys. Status Solidi RRL – Rapid Res. Lett.* **14**, 2000381 (2020).
30. Ci, P. et al. Chemical trends of deep levels in van der Waals semiconductors. *Nat. Commun.* **11**, 5373 (2020).
31. Ma, N. & Jena, D. Carrier statistics and quantum capacitance effects on mobility extraction in two-dimensional crystal semiconductor field-effect transistors. *2D Mater.* **2**, 015003 (2015).
32. Fang, N. & Nagashio, K. Band tail interface states and quantum capacitance in a monolayer molybdenum disulfide field-effect transistor. *J. Phys. Appl. Phys.* **51**, 065110 (2018).
33. Yamasaki, K., Yoshida, M. & Sugano, T. Deep Level Transient Spectroscopy of Bulk Traps and Interface States in Si MOS Diodes. *Jpn. J. Appl. Phys.* **18**, 113 (1979).
34. Coelho, A. V. P., Adam, M. C. & Boudinov, H. Distinguishing bulk traps and interface states in deep-level transient spectroscopy. *J. Phys. Appl. Phys.* **44**, 305303 (2011).

35. Weiss, S. & Kassing, R. Deep Level Transient Fourier Spectroscopy (DLTFS)—A technique for the analysis of deep level properties. *Solid-State Electron* **31**, 1733–1742 (1988).
36. Li, J. V. & Ferrari, G. *Capacitance Spectroscopy of Semiconductors*. (Jenny Stanford Publishing, 2018). <https://doi.org/10.1201/b22451>.
37. Grillot, P. N., Ringel, S. A., Fitzgerald, E. A., Watson, G. P. & Xie, Y. H. Electron trapping kinetics at dislocations in relaxed Ge_{0.3}Si_{0.7}/Si heterostructures. *J. Appl. Phys.* **77**, 3248–3256 (1995).
38. Vancsó, P. et al. The intrinsic defect structure of exfoliated MoS₂ single layers revealed by Scanning Tunneling Microscopy. *Sci. Rep.* **6**, 29726 (2016).
39. Shree, S. et al. High optical quality of MoS₂ monolayers grown by chemical vapor deposition. *2D Mater.* **7**, 015011 (2019).
40. Dumcenco, D. et al. Large-Area Epitaxial Monolayer MoS₂. *ACS Nano* **9**, 4611–4620 (2015).
41. Kresse, G. & Furthmüller, J. Efficient iterative schemes for ab initio total-energy calculations using a plane-wave basis set. *Phys. Rev. B* **54**, 11169–11186 (1996).
42. Perdew, J. P., Burke, K. & Ernzerhof, M. Generalized Gradient Approximation Made Simple. *Phys. Rev. Lett.* **77**, 3865–3868 (1996).
43. Kresse, G. & Joubert, D. From ultrasoft pseudopotentials to the projector augmented-wave method. *Phys. Rev. B* **59**, 1758–1775 (1999).
44. Blöchl, P. E. Projector augmented-wave method. *Phys. Rev. B* **50**, 17953–17979 (1994).
45. Li, H. et al. Activating and optimizing MoS₂ basal planes for hydrogen evolution through the formation of strained sulphur vacancies. *Nat. Mater.* **15**, 48–53 (2016).

Acknowledgements

We acknowledge Z. Sun, A. Ciarrocchi, J. Zhang, and G. M. Marega for discussions. We thank the help of Z. Benes (CMI) with electron-beam lithography. Device fabrication was carried out at the EPFL Center for micro and nanotechnology. Electron microscopy imaging was performed at the EPFL Interdisciplinary Centre for Electron Microscopy. This work was financially supported by the European Union's Horizon 2020 research and innovation program under grant agreements No. 785219 and 881603 (Graphene Flagship Core 2 and Core 3), No. 829035 (QUEFORMAL), No. 964735 (EXTREME-IR), European Research Council (grants no. 682332 and 899775), the Swiss National Science Foundation (grants no. 175822, 157739), the CCMX Materials Challenge grant "Large area growth of 2D materials for device integration". KC and O.V.Y acknowledge the support by the Swiss National Science Foundation (grant no. 172534), A.A acknowledges support from the Singapore National Research Foundation under NRF Fellowship (grant no. NRFF14-2022-0083). Calculations were performed at the facilities of Scientific IT and Application Support Center of EPFL and the Swiss National Supercomputing Centre (CSCS) under project s1008.

Author contributions

A.K. initiated and supervised the project. Y.Z. and A.K. designed the experiments. Y.Z. fabricated the device, performed the C-V and DLTS measurement, and derived the 2D Arrhenius functions for calculations. M.T. performed STEM imaging, simulations, and defect concentration calculations. K.C. and O.V.Y. devised the models, and performed the first-principles calculations and plotting. Y.Z. performed the Ar plasma irradiation test and treatment. Y.Z. and J.F.G.M. fabricated the control device with transferred metal contact. Y.Z., A.A, and A.K. analyzed the data with input from J.F.G.M. and C.Y.C. Y.Z. and H.G.J. prepared the MOCVD-grown MoS₂ monolayer. Z.W. performed Raman spectroscopy. Y.Z., A.A., H.G.J., and A.K. wrote the manuscript with input from M.T. and K.C.

Competing interests

The authors declare no competing interests.

Additional information

Supplementary information The online version contains supplementary material available at <https://doi.org/10.1038/s41467-022-35651-1>.

Correspondence and requests for materials should be addressed to Andras Kis.

Peer review information *Nature Communications* thanks Yaping Dan, Robert Kudrawiec and the other, anonymous, reviewer(s) for their contribution to the peer review of this work.

Reprints and permissions information is available at <http://www.nature.com/reprints>

Publisher's note Springer Nature remains neutral with regard to jurisdictional claims in published maps and institutional affiliations.

Open Access This article is licensed under a Creative Commons Attribution 4.0 International License, which permits use, sharing, adaptation, distribution and reproduction in any medium or format, as long as you give appropriate credit to the original author(s) and the source, provide a link to the Creative Commons license, and indicate if changes were made. The images or other third party material in this article are included in the article's Creative Commons license, unless indicated otherwise in a credit line to the material. If material is not included in the article's Creative Commons license and your intended use is not permitted by statutory regulation or exceeds the permitted use, you will need to obtain permission directly from the copyright holder. To view a copy of this license, visit <http://creativecommons.org/licenses/by/4.0/>.

© The Author(s) 2023